



A New Halocarbon Absorption Model Based on HITRAN Cross-Section Data and New Estimates of Halocarbon Instantaneous Clear-Sky Radiative

Downloaded from: <https://research.chalmers.se>, 2025-12-04 17:03 UTC

Citation for the original published paper (version of record):

Buehler, S., Brath, M., Lemke, O. et al (2022). A New Halocarbon Absorption Model Based on HITRAN Cross-Section Data and New Estimates of Halocarbon Instantaneous Clear-Sky Radiative Forcing. *Journal of Advances in Modeling Earth Systems*, 14(11). <http://dx.doi.org/10.1029/2022MS003239>

N.B. When citing this work, cite the original published paper.

RESEARCH ARTICLE

10.1029/2022MS003239

Key Points:

- A new polynomial model for laboratory absorption cross-section data was developed
- The new model was used to compute instantaneous clear-sky halocarbon radiative efficiencies and present day radiative forcing
- Halocarbons are found to contribute approximately 20% of the total anthropogenic instantaneous clear-sky forcing

Correspondence to:

S. A. Buehler,
stefan.buehler@uni-hamburg.de

Citation:

Buehler, S. A., Brath, M., Lemke, O., Hodnebrog, Ø., Pincus, R., Eriksson, P., et al. (2022). A new halocarbon absorption model based on HITRAN cross-section data and new estimates of halocarbon instantaneous clear-sky radiative forcing. *Journal of Advances in Modeling Earth Systems*, 14, e2022MS003239. <https://doi.org/10.1029/2022MS003239>

Received 10 JUN 2022






Accepted 1 NOV 2022

Author Contributions:

Conceptualization: Stefan A. Buehler
Data curation: Oliver Lemke
Formal analysis: Manfred Brath
Methodology: Stefan A. Buehler, Robert Pincus
Software: Manfred Brath, Oliver Lemke, Patrick Eriksson, Richard Larsson
Validation: Øivind Hodnebrog
Visualization: Manfred Brath, Oliver Lemke
Writing – original draft: Stefan A. Buehler
Writing – review & editing: Stefan A. Buehler, Manfred Brath, Oliver Lemke, Øivind Hodnebrog, Robert Pincus, Patrick Eriksson, Iouli Gordon, Richard Larsson

© 2022 The Authors. Journal of Advances in Modeling Earth Systems published by Wiley Periodicals LLC on behalf of American Geophysical Union. This is an open access article under the terms of the [Creative Commons Attribution License](#), which permits use, distribution and reproduction in any medium, provided the original work is properly cited.

A New Halocarbon Absorption Model Based on HITRAN Cross-Section Data and New Estimates of Halocarbon Instantaneous Clear-Sky Radiative Forcing

Stefan A. Buehler¹ , Manfred Brath¹ , Oliver Lemke¹ , Øivind Hodnebrog² , Robert Pincus³ , Patrick Eriksson⁴ , Iouli Gordon⁵ , and Richard Larsson¹

¹Meteorologisches Institut, Centrum für Erdsystem- und Nachhaltigkeitsforschung (CEN), Fachbereich Erdsystemwissenschaften, Fakultät für Mathematik, Informatik und Naturwissenschaften, Universität Hamburg, Hamburg, Germany, ²Center for International Climate Research (CICERO), Oslo, Norway, ³Lamont-Doherty Earth Observatory, Columbia University, Palisades, NY, USA, ⁴Department of Space, Earth and Environment, Chalmers University of Technology, Gothenburg, Sweden, ⁵Atomic and Molecular Physics Division, Center for Astrophysics, Harvard & Smithsonian, Cambridge, MA, USA

Abstract The article describes a new practical model for the infrared absorption of chlorofluorocarbons and other gases with dense spectra, based on high-resolution transmission molecular absorption database (HITRAN) absorption cross-sections. The model is very simple, consisting of frequency-dependent polynomial coefficients describing the pressure and temperature dependence of absorption. Currently it is implemented for the halocarbon species required by the Radiative Forcing Model Intercomparison Project. In cases where cross-section data is available at a range of different temperatures and pressures, this approach offers practical advantages compared to previously available options, and is traceable, since the polynomial coefficients follow directly from the laboratory spectra. The new model is freely available and has several important applications, notably in remote sensing and in developing advanced radiation schemes for global circulation models that include halocarbon absorption. For demonstration, the model is applied to the problem of computing instantaneous clear-sky halocarbon radiative efficiencies and present day radiative forcing. Results are in reasonable agreement with earlier assessments that were carried out with the less explicit Pinnock method, and thus broadly validate that method. Plain Language Summary Chlorofluorocarbons and other related gases have dense and complicated absorption spectra that can be measured in the laboratory. We bring such measurements to a form that can be used for simulations of the transfer of radiation through the atmosphere. Then we use the new model to calculate new estimates of the climate impact of these man-made gases. The results broadly validate earlier calculations that were done with a less explicit method.

Plain Language Summary Chlorofluorocarbons and other related gases have dense and complicated absorption spectra that can be measured in the laboratory. We bring such measurements to a form that can be used for simulations of the transfer of radiation through the atmosphere. Then we use the new model to calculate new estimates of the climate impact of these man-made gases. The results broadly validate earlier calculations that were done with a less explicit method.

1. Introduction

In this work, we present a simple new model of halocarbon absorption, based on laboratory measurements collected by high-resolution transmission molecular absorption database (HITRAN) (Gordon et al., 2017; Kochanov et al., 2019), and use it to estimate present-day (PD) instantaneous clear-sky halocarbon climate forcing and radiative efficiencies (REs) of the different compounds.

The need for the new model arises because spectroscopic data to date come in two different forms, depending on molecular species. The more fundamental form is as catalogs of spectral line parameters, from which the total absorption cross-section for arbitrary frequency, pressure and temperature can be calculated as the sum over all spectral lines. But such catalogs are not yet available for many molecular species with dense spectra.

The other form of data are as measured absorption cross-sections at a discrete set of pressures (p) and temperatures (T). This solves the problem of not being able to handle the complexity of the line spectrum, but instead raises the problem how to estimate absorption for p/T conditions that are different from those of the measurements. In the atmosphere, variations in p and T are large (five orders of magnitude for p and still 100 K or 50% for T), and in

general one has to know the local absorption cross-sections in order to simulate the radiative transfer through the atmosphere accurately. This requires the discrete absorption cross-section data to be cast into the form of a model that provides absorption as a continuous function of frequency, p and T , just like the calculation from spectral line parameters does for species for which it is available. Such a model has many applications, for example, in remote sensing, in generating k -distributions for circulation model radiation schemes, and in estimating radiative forcing.

Some available radiative transfer (RT) models, such as Line-By-Line Radiative Transfer Model (LBLRTM) (Clough et al., 2005) and SFIT (Hase et al., 2004) do already contain such functions internally for selected molecules, but the list has been incomplete and the implementation of these models has not been very transparent, so that we see the need for a new model. For this purpose, we transform the HITRAN laboratory cross-sections data (Gordon et al., 2017) into an absorption model by a simple second-order polynomial fit. This is done for all absorption species that are part of the Radiative Forcing Model Intercomparison Project (RFMIP) experiment (Pincus et al., 2016) in Coupled Model Intercomparison Project 6 (CMIP6) (Eyring et al., 2016). Almost all, that is, since we treat two species (CH_3Cl and CH_3Br) by explicit spectral line calculations, and one species (C_7F_{16}) not at all, because there is neither spectral line nor cross-section data available from HITRAN. The specification of gas concentrations in RFMIP follows the more general CMIP specification for concentrations (Meinshausen et al., 2017).

As a test and demonstration of the new model we consider the problem of estimating radiative forcing by halocarbons and related chemical compounds, which is an important part of the total anthropogenic climate forcing. Existing assessments (see review in Hodnebrog, Aamaas, et al. (2020)) are based on the Pinnock method (Pinnock et al., 1995). In that method, forcing at some reference level (usually the tropopause (TRP)) is pre-calculated for an artificial absorber that absorbs weakly with the same cross-section at all frequencies, and this is done for a dense frequency grid, obtaining what we call the Pinnock forcing curve. Forcing for an arbitrary molecular species can then be estimated by multiplying the Pinnock curve with the measured absorption cross-section of that species. The newest elaboration even takes into account stratospheric temperature adjustment in the Pinnock curve (Shine & Myhre, 2020), so that the method is one step closer to providing the effective radiative forcing (Hodnebrog, Myhre, et al., 2020). Furthermore, the Pinnock method can easily include clouds, and, as time goes on, has used ever higher spectral resolution.

While this method is very efficient and has the great advantage of not requiring a radiative transfer code to compute forcings, it has the disadvantage of using only the laboratory measurement at a single pressure and temperature. Often the measurement closest to surface (SRF) pressure and room temperature is used, since the experimental uncertainties are typically smallest under those conditions. While it is easy to repeat the calculation with a different spectrum, the method in its present form can not account for the fact that the local absorption spectrum at different altitudes in reality depends on the local pressure and temperature. The method could probably be extended to take these variations into account, in analogy to the radiative kernel method that is used to diagnose radiative feedbacks and adjustments in climate models (Soden & Held, 2006), but that would significantly increase its computational cost and complexity. Alternatively, in cases where laboratory measurements for different conditions are available, it could in principle be optimized which measurement is used, so as to get the most accurate forcing.

Furthermore, radiative forcing has been shown to depend strongly on the atmospheric state at different locations on the globe (Huang et al., 2016) not just through the temperature dependence of the Planck function which governs emission, but also through the temperature dependence of absorption, and these dependencies are difficult to represent in the Pinnock method, which typically uses just a few atmospheres.

Here we apply the new halocarbon absorption model to a set of 100 reference atmospheres to compute new estimates of the global mean instantaneous clear-sky radiative forcing by halocarbons with the radiative transfer model Atmospheric Radiative Transfer Simulator (ARTS) (Buehler et al., 2005, 2018; Eriksson et al., 2011). For simplicity, we refer to the new halocarbon model also with the name “ARTS” below, where it is necessary to distinguish it from other models. But the halocarbon model itself is constructed such that it can be easily used in other radiative transfer models as well.

Note that we do not make the claim that the method of direct calculation that we apply is in general to be preferred over the Pinnock method for estimating radiative forcing. That method has many practical advantages, as outlined above, not the least that it allows anyone to estimate the forcing of a given species easily, without access to a radiative transfer model. Rather, we pick this application as one example of the many anticipated uses of the new absorption model.

The paper is structured as follows: Section 2 describes the new absorption model and the philosophy behind it. Section 3 presents new estimates of instantaneous clear-sky radiative efficiency and PD radiative forcing, based on our model and the RFMIP/CMIP gas concentrations. Section 4 contains the summary and conclusions.

2. Absorption Model

2.1. HITRAN Data

As outlined above, for many heavy polyatomic molecules, it is very difficult to provide accurate line-by-line lists due to the complexity of their spectra, and therefore an acceptable alternative practice is to publish absorption cross-sections at different pressures and temperatures, measured in the laboratory. Large sets of such data are described by Sharpe et al. (2004), Johnson et al. (2010) and Hodnebrog et al. (2013). HITRAN (the high-resolution transmission molecular absorption database) draws on such compilations, and complements them with numerous individual measurements from the literature, in order to provide measured absorption cross-sections for almost 300 different gas molecules. (Another database that systematically collects cross-sections in this way is Gestion et Etude des Informations Spectroscopiques Atmosphériques: Management and Study of Atmospheric Spectroscopic Information (Jacquinet-Husson et al., 2016), but our study is based on the HITRAN data).

These HITRAN cross-section data are described in detail in Gordon et al. (2017). We use the HITRAN2016 version. Note that a new version of HITRAN has become available since our model was implemented (HITRAN2020, released in October 2021, Gordon et al., 2022), featuring a few updates in cross-sections with respect to HITRAN2016. For instance, CFC-11 data were updated with recent measurements from Harrison (2018).

The structure of the data is such that for each absorption species there are data in one or more spectral bands, and for each spectral band there can be data at several pressure/temperature pairs. Note that the pressure here is practically identical to the pressure of the broadening gas, since the absorption species concentration is so low that its contribution to the total pressure is practically negligible. Some of the laboratory data were measured with air as broadening gas, some with pure nitrogen, and for some HITRAN does not specify this. In the ARTS implementation as well, the pressure is always the total pressure (for line-by-line species there is an option to treat different broadening gases explicitly, where data are available, but this option is not available for the new cross-section species).

As an example for the data, Figure 1 shows one of the absorption bands for CFC11. This is one of the best-covered species, and the figure also shows the pressures and temperatures of the available CFC11 spectra for the band. Coverage can be much poorer for other species as shown in Figure 2. HALON1301, for example, is available at three different temperatures, but only ambient pressure, and HFC236fa has only a single measured spectrum at ambient pressure and temperature.

HITRAN does not state uncertainty estimates for these data. Taking CFC11 as example, comparison of the different available literature data sets given in the appendix of Hodnebrog, Aamaas, et al. (2020) shows differences in integrated absorption cross-section of approximately 20% between the highest and lowest data set, but some of these measurements are quite old. The same paper suggests a general estimate of 5% for experimental uncertainty of the latest laboratory data, plus 3% for missing far infrared absorption bands. These estimates are for the radiative efficiency, but since this scales directly with the integrated absorption cross-section, we here also assume around 8% experimental uncertainty for the integrated absorption cross-section. (Note that Hodnebrog, Aamaas, et al. (2020) additionally suggest a 5% uncertainty for missing shortwave bands, which we ignore here because our focus is only on the longwave).

2.2. Modeling Strategies

To use these data in an RT simulation, it is necessary to provide an estimate of the absorption at arbitrary frequency, temperature, and pressure, within reasonable limits, not just at the discrete points of the laboratory measurements. This is a practical challenge, since data often are rather sparsely sampled in pressure and temperature.

One approach to solve this is to start with a laboratory measurement at low pressure, and convolve it with a Lorentz function with a pressure dependent width to mimic the effect of pressure broadening. This approach, which we will refer to as the *convolution method*, is for example, taken in LBLRTM (Clough et al., 2005).

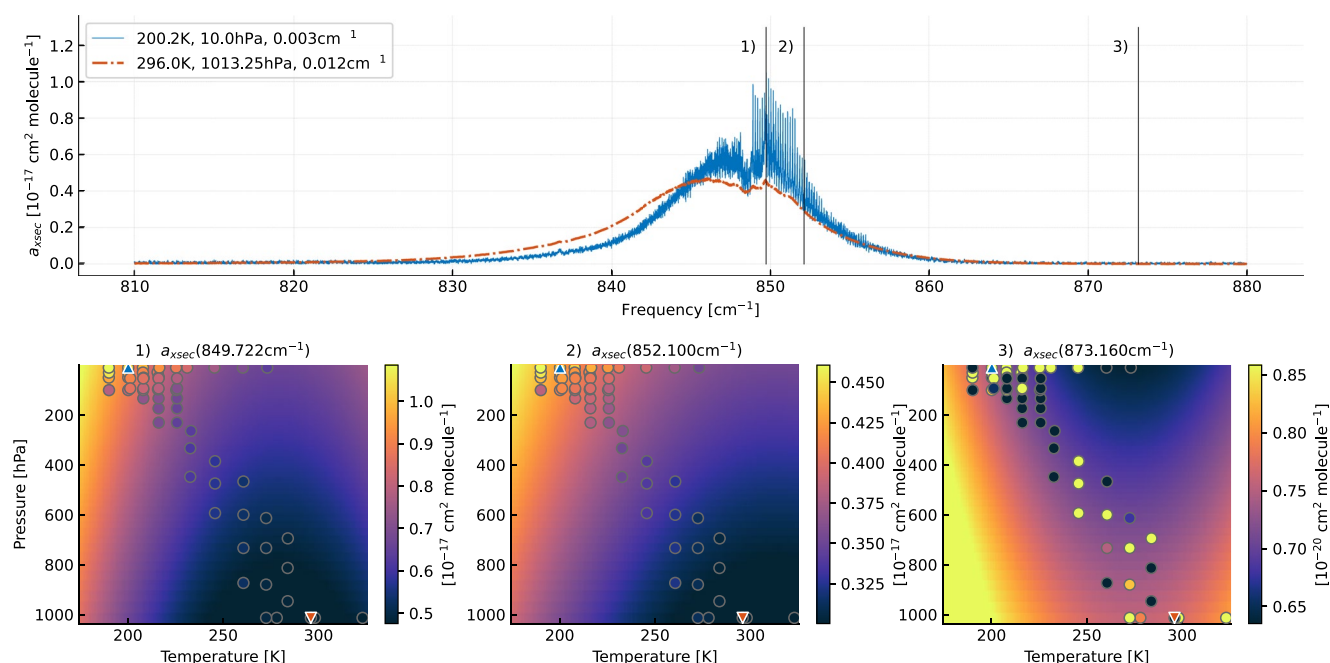


Figure 1. HITRAN laboratory absorption cross-section data of CFC11. The frequency unit is Kayser (sometimes called wavenumber) in cm^{-1} , following the convention in the field. The black vertical lines denote the frequencies of the three bottom plots. Bottom plots show fitted absorption cross-section as function of T and p . The circles denote the cross-sections from HITRAN laboratory data. The triangles show the position in pressure and temperature space of the spectra shown in the top plot. Note that the apparent discrepancies in the HITRAN data in the rightmost bottom plot represent noise, since the top plot shows that the absolute value there is very small.

We started out this project by systematically implementing the convolution method, that is, we set up a simple model for the pressure dependence of the width (linear with a breakpoint) and determined suitable parameters for this model for those data sets with sufficient coverage of the laboratory data in pressure (p)/temperature (T) space. For other species we used a default pressure dependence.

This approach worked, but we were not fully satisfied with it. There are two main drawbacks: First, it is challenging to account for the temperature dependence, because the sampling of the available laboratory spectra in p/T space is so irregular that neither temperature interpolation before the convolution nor after the convolution gives reliable results in all cases. For example, it sometimes introduces artificial negative values. The second drawback of the convolution method is that it uses only a small part of the laboratory data for the actual model, since it relies heavily on the single low pressure reference spectrum.

We therefore also investigated the less physical and more pragmatic approach of fitting a suitable simple *polynomial model* to the entire set of measurements for a given species. This approach gives more accurate results, judged by how accurately the model reproduces the measurements and how well-behaved it is in those areas of p/T space that are not covered by any measurements. Based on these tests, the convolution method was given up and the polynomial model was selected as standard. It is described in more detail below. The approach of fitting a polynomial model is fairly common practice for ultraviolet absorption cross-sections (e.g., Equation 1 in Bak et al., 2020), but as far as we know has not yet been used for the infrared spectral range. In the ultraviolet case it is only the temperature dependence that is fitted, since pressure broadening is much less relevant than in the infrared, due to the dominant Doppler broadening.

An interesting alternative to our approach is the pseudo-line method (PL method from here on). In the PL method, the measured cross-sections are interpolated by a set of pseudo spectral lines, parameters of which are fitted so that they reproduce the measurements. This approach is quite wide-spread in remote sensing with Fourier transform instruments (e.g., Rinsland et al., 1985) and used in the popular SFIT retrieval software (Hase et al., 2004). However, PL parameters are not readily available for most of the halocarbon species investigated here.

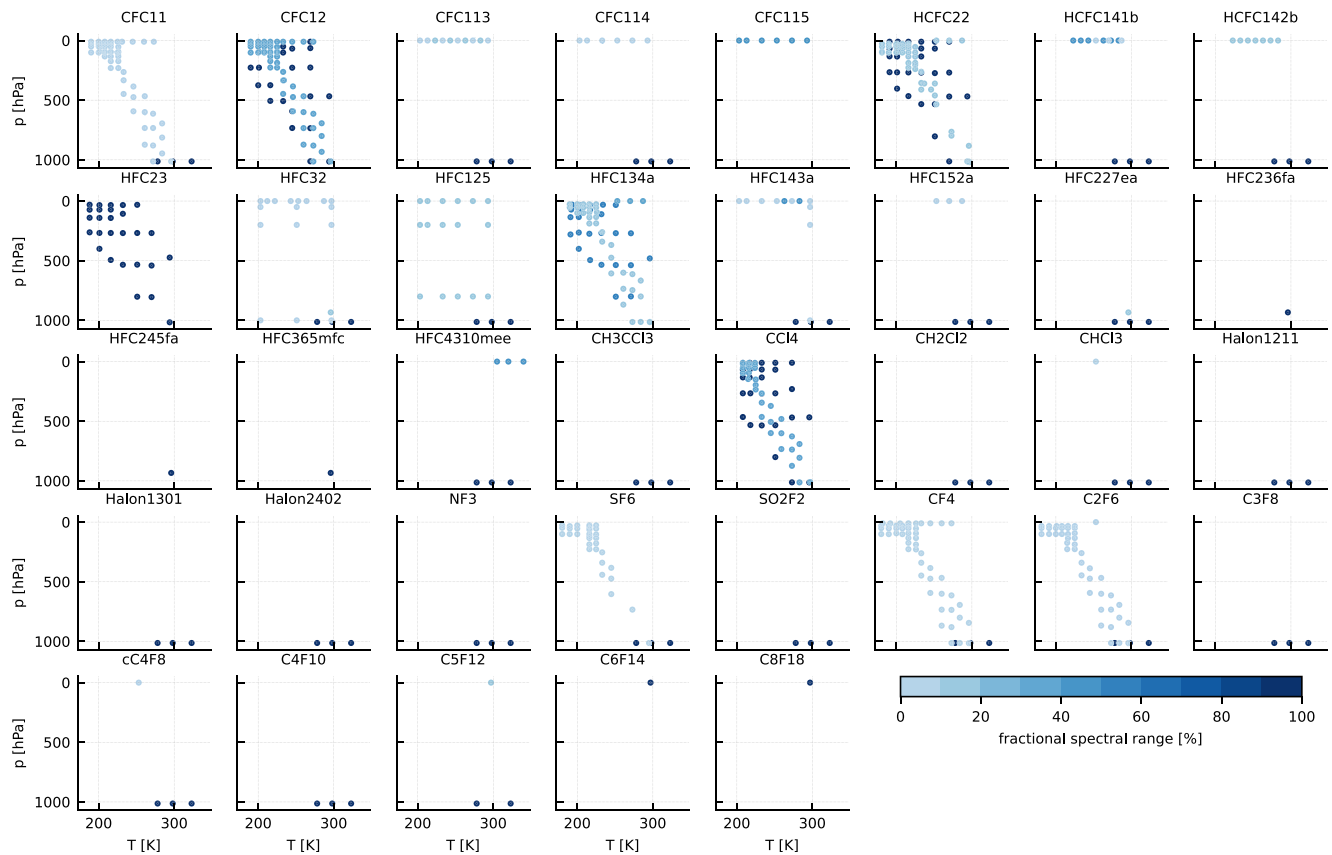


Figure 2. HITRAN absorption cross-section spectra for relevant molecules. Each dot represents an available spectrum. Spectra have varying frequency coverage. The shading indicates the spectral range of each spectrum in relation to the spectral range of the fit. For example, in the case of CFC11 some of the surface temperature spectra have a wide spectral range, which defines the range of our model (100%). The other spectra, shaded in light blue, cover only less than 10% of this range.

Rather than attempting to derive new PL parameters for the HITRAN cross-section data, we chose the polynomial fit method for its greater simplicity, which makes the problem of deriving the parameterization simultaneously for a long list of species tractable, whereas the PL method, at least in its present form, seems to need some expert judgment for each individual species. It would also need partition functions, which are not readily available for most of the species considered here.

2.3. The Polynomial Model

The basic idea is to set up a simple model for the pressure and temperature dependence of the absorption species, and then apply a global fit to all the available laboratory spectra for a given species. This is done separately for all frequencies where laboratory data are available. Explicitly, for a given species and at a given frequency ν , the observed cross-section $\sigma(T, p)$ is fitted in temperature T and pressure p by an up to second order polynomial:

$$\sigma = c_{00} + c_{10}x + c_{01}y + c_{20}x^2 \quad (1)$$

with

$$x = \frac{T}{T_0}, \quad (2)$$

and

$$y = \frac{p}{p_0}, \quad (3)$$

Table 1
Fitting Conditions for the Cross-Section Fit

Fit model	$N_{T,\min}$	$N_{p,\min}$	N_{\min}	$\max(p) - \min(p) \geq$	$\max(T) - \min(T) \geq$
$c_{00} + c_{10}x + c_{01}y + c_{20}x^2$	5	2	6	800 hPa	80 K
$c_{00} + c_{10}x + c_{01}y$	2	2	4	800 hPa	40 K
$c_{00} + c_{10}x + c_{20}x^2$	5	1	5	0 hPa	80 K
$c_{00} + c_{10}x$	3	1	3	0 hPa	40 K
$c_{00} + c_{01}y$	1	3	3	800 hPa	0 K
c_{00}	1	1	1	0 hPa	0 K

Note. Variables x and y are defined according to Equations 2 and 3. Columns $N_{T,\min}$, $N_{p,\min}$ and N_{\min} state the minimum required number of laboratory cross-section spectra in T , in p and in total. The last two columns state the required range in p and T , respectively.

using a least squares fit. The variables $T_0 = 1$ K and $p_0 = 1$ Pa are constant factors to remove the units of T and p . The coefficients c_{ij} and the cross-section σ are defined in units of $[\text{m}^2]$ (ARTS internally uses SI units where possible). The frequency dimension was omitted in the above equations for brevity, but note that the coefficients are given for a discrete set of frequencies. When the model is applied, absorption has to be interpolated in frequency between these discrete points.

The fitting process includes a simple outlier detection algorithm.

1. Fit the data using all given data at frequency ν .
2. Estimate the residuals between fit and data.
3. Fit the data excluding all data points with residuals $> 1.5 \sigma_{\text{data}}$ in which σ_{data} is the standard deviation of the data at given frequency

The HITRAN cross-section data are very diverse in their spectral resolution, and in p/T coverage, as discussed in detail in Kochanov et al. (2019). For example, there are species that have high p/T resolution data in a specific spectral range and only coarse p/T resolution data outside that range. Frequency resolution also varies considerably in different parts of the spectrum. Spectra cover different frequency ranges, sometimes overlapping. Since the number of observations at different temperatures and pressures varies over the spectral range, the fitting model is selected for each frequency individually, as summarized in Table 1.

One advantage of this method is that the use of the absorption model in an RT code is extremely simple, basically just using Equation 1 with our tabulated fit coefficient data, where missing coefficients are set to zero. The evaluation of the model is computationally cheap, since no expensive operations, such as convolutions, are needed. In a final step, absorption cross-sections are linearly interpolated in frequency between the discrete model points.

Extrapolation is always more dangerous than interpolation, but we selected the interpolation order such that it is safe to use the new polynomial model also outside the p/T range of the laboratory measurements. This simplifies the implementation of the model, for example, in a radiative transfer code.

One caveat is that negative absorption cross-sections can occur, both inside and outside the laboratory temperature and pressure range. Inside, the negative values occur only at the noise level of the absorption spectra. Outside, more negative values are possible due to the extrapolation. To account for both issues, negative absorption cross-sections are simply set to zero when the model is applied. To avoid a positive bias due to the removal of negative values, the spectrum is scaled afterward so that the integral over the spectrum of the specific band does not change.

To fit the polynomial model, input data have to be harmonized with respect to their frequency grids. The basic idea is to use the highest spectral resolution of the set of observations of a species and use this resolution as the reference resolution. The observations with coarser frequency resolution are linearly interpolated onto this resolution.

Some molecular species have a very high resolution for a small spectral range, and coarse resolution or no data elsewhere. An interpolation to a uniform high-resolution grid therefore would be wasteful, and instead the data

Table 2

Considered Cross-Section Species Together With Spectral, Pressure and Temperature Limits and With $O_{p,T}$ the Maximum Polynomial Order of the Pressure/Temperature Dependency of the Band (Continued in Next Table)

Species	Band	$\tilde{\nu}_{\min}$ [cm ⁻¹]	$\tilde{\nu}_{\max}$ [cm ⁻¹]	$\delta\tilde{\nu}$ [cm ⁻¹]	p_{\min} [hPa]	p_{\max} [hPa]	T_{\min} [K]	T_{\max} [K]	O_p	O_T
CFC11	0	570	810	0.060	1013.25	1013.25	278.10	323.10	0	1
	1	810	880	0.003	10.00	1013.25	190.00	323.10	1	2
	2	880	1050	0.060	1013.25	1013.25	278.10	323.10	0	1
	3	1,050	1,120	0.003	10.00	1013.25	190.00	323.10	1	2
	4	1,120	6,500	0.060	1013.25	1013.25	278.10	323.10	0	1
CFC12	0	800	1,270	0.001	10.00	1014.58	189.50	296.30	1	2
CFC113	0	600	1,250	0.015	0.00	1013.25	203.00	323.10	1	2
	1	1,250	5,000	0.060	1013.25	1013.25	278.10	323.10	0	1
CFC114	0	600	815	0.060	1013.25	1013.25	278.10	323.10	0	1
	1	815	860	0.015	0.00	1013.25	203.00	323.10	1	2
	2	860	870	0.060	1013.25	1013.25	278.10	323.10	0	1
	3	870	960	0.015	0.00	1013.25	203.00	323.10	1	2
	4	960	1,030	0.060	1013.25	1013.25	278.10	323.10	0	1
	5	1,030	1,067	0.015	0.00	1013.25	203.00	323.10	1	2
	6	1,067	1,095	0.060	1013.25	1013.25	278.10	323.10	0	1
	7	1,095	1,285	0.015	0.00	1013.25	203.00	323.10	1	2
CFC115	8	1,285	5,000	0.060	1013.25	1013.25	278.10	323.10	0	1
	0	955	1,015	0.015	0.00	0.00	203.00	293.00	0	2
	1	1,110	1,145	0.015	0.00	0.00	203.00	293.00	0	2
HCFC22	2	1,167	1,260	0.015	0.00	0.00	203.00	293.00	0	2
	0	730	1,380	0.001	0.00	1019.38	181.00	297.00	1	2
	0	550	560	0.060	1013.25	1013.25	278.10	323.10	0	1
HCFC141b	1	560	3,100	0.008	0.00	1013.25	223.00	323.10	1	2
	2	3,100	6,500	0.060	1013.25	1013.25	278.10	323.10	0	1
HCFC142b	0	600	650	0.060	1013.25	1013.25	278.10	323.10	0	1
	1	650	1,500	0.008	0.00	1013.25	223.00	323.10	1	2
	2	1,500	6,500	0.060	1013.25	1013.25	278.10	323.10	0	1
HFC23	0	950	1,500	0.001	30.66	1016.45	187.60	294.40	1	2
HFC32	0	400	450	0.120	933.26	933.26	296.00	296.00	0	0
	1	450	630	0.017	0.00	1013.25	253.00	323.10	1	1
	2	630	995	0.060	933.26	1013.25	278.10	323.10	0	1
	3	995	1,236	0.015	0.00	1013.25	203.00	323.10	1	2
	4	1,236	1,385	0.060	933.26	1013.25	278.10	323.10	0	1
	5	1,385	1,475	0.015	0.00	1013.25	203.00	323.10	1	2
HFC125	6	1,475	6,500	0.060	1013.25	1013.25	278.10	323.10	0	1
	0	495	495	0.048	0.00	0.00	253.00	253.00	0	0
	1	495	499	0.048	0.00	799.93	203.00	273.00	0	1
	2	499	1,504	0.048	0.00	1013.25	203.00	323.10	1	2
HFC134a	3	1,504	6,500	0.060	1013.25	1013.25	278.10	323.10	0	1
	0	75	590	0.017	0.00	0.00	253.00	253.00	0	0
	1	600	750	0.015	0.00	0.00	253.00	253.00	0	0
	2	750	1,600	0.001	0.00	1014.32	190.00	296.00	1	2

Table 2
Continued

Species	Band	$\tilde{\nu}_{\min}$ [cm ⁻¹]	$\tilde{\nu}_{\max}$ [cm ⁻¹]	$\delta\tilde{\nu}$ [cm ⁻¹]	p_{\min} [hPa]	p_{\max} [hPa]	T_{\min} [K]	T_{\max} [K]	O_p	O_T
HFC143a	0	500	550	0.060	1013.25	1013.25	278.10	323.10	0	1
	1	550	3,500	0.008	0.00	1013.25	203.00	323.10	1	2
	2	3,500	6,500	0.060	1013.25	1013.25	278.10	323.10	0	1
HFC152a	0	525	830	0.060	1013.25	1013.25	278.10	323.10	0	1
	1	830	840	0.010	0.00	1013.25	253.00	323.10	1	1
	2	840	995	0.009	0.00	1013.25	253.00	323.10	1	1
	3	995	1,050	0.010	0.00	1013.25	253.00	323.10	1	1
	4	1,050	1,205	0.009	0.00	1013.25	253.00	323.10	1	1
	5	1,205	1,320	0.010	0.00	1013.25	253.00	323.10	1	1
	6	1,320	1,490	0.009	0.00	1013.25	253.00	323.10	1	1
	7	1,490	1,500	0.010	0.00	1013.25	253.00	323.10	1	1
HFC227ea	0	400	500	0.121	933.26	933.26	296.00	296.00	0	0
	1	500	6,500	0.060	933.26	1013.25	278.10	323.10	0	1
HFC236fa	0	350	1,500	0.120	933.26	933.26	296.00	296.00	0	0
HFC245fa	0	640	1,500	0.241	933.26	933.26	296.00	296.00	0	0
HFC365mfc	0	600	2,000	0.060	933.26	933.26	296.00	296.00	0	0

are split into bands of different spectral resolution. Tables 2 and 3 list the implemented species, their bands, and for each band the p/T limits of the laboratory data and the polynomial orders in p and T that were adopted.

A good measure for the overall absorption strength of a molecule is the frequency-integrated absorption cross-section S . Table 4 lists this for our new polynomial model (“ARTS”) and the raw HITRAN laboratory spectra. For ARTS we use 293 K and 1013.25 hPa, for HITRAN the spectra closest to these conditions. The new model does not agree exactly with the individual raw spectra, since spectra at other pressures and temperatures also influence the polynomial coefficients. Discrepancies are mostly below 1%, but in a few cases around 3%–5% and in one case (HFC32) as large as approximately 7%.

We interpret these discrepancies as indications of inconsistency in the laboratory spectra at different temperatures or pressures, rather than an indication of inadequacy of the polynomial model. This suggests that the ARTS-HITRAN differences in Table 4 can be taken as an uncertainty estimate of our model for individual species, in addition to the general 5% uncertainty on laboratory cross-section data mentioned in Section 2.1.

The problem of fit consistency and data homogeneity is illustrated by Figure 3, showing S as a function of T for two different species. Note that the fit of the model is done for each individual frequency, and that the model curves shown in the figure emerge by integrating the model that is thus derived over frequency. Likewise, the measurement points are derived by integrating the measured spectra. Hence, the curves in the figure do not represent direct fits to the points in the figure, rather a consistency check of the underlying individual fits. From line-by-line theory, we would expect S to be independent of temperature, because changing temperature changes the population of molecular energy levels, which strengthens some lines and weakens others, depending on the energy states involved, and additionally the partition function ratio accounts for the change in the number of active levels with temperature (see Equations 3 and 4 in Buehler et al. (2005) and associated text).

We can thus use S as a sanity check and guard against overfitting. As Figure 3 shows, the quadratic fit is reasonable for CFC11 where there is a wealth of laboratory data. Despite the strong temperature dependence at individual frequencies as shown in Figure 1, the temperature dependence of S is weak, approximately 3% across the temperature range, consistent with the laboratory data. Pressure dependence of S is also very weak, as expected. (Pressure broadening does not change the integral under individual spectral lines, but still S can vary slightly on pressure due to the numerics of integrating over a finite set of frequencies).

In contrast to CFC11, Halon1301 has only three measurements, near 280 K, 300 and 320 K. The middle one has a much lower S value. Taking this at face value leads to a strong T dependence, so strong that it would impact forcing estimates significantly, even if one were to extrapolate linearly outside the T range of the data. We judge this to be implausible, so we instead select the linear fit for this species, leading to a higher fit residual, and a model with hardly any T dependence. Together with the model data (see Section 5), we distribute a supplement with figures similar to Figure 3 for all included species. Variations in S across the atmospheric temperature range are below approximately 10%, the supplement can be used to check this for individual species.

Another reason for larger discrepancies in some cases are ambiguities in which of the laboratory spectra to use for the S_{HITRAN} calculation, since different spectral data sets have different p/T ranges, as shown in Table 2. The spectrum closest to ambient conditions may not cover the full spectral range. The algorithm that we use is that we split the HITRAN spectra according to our defined frequency bands. For each band we take the HITRAN data set that is closest to ambient conditions and covers at least 90% of the band. Note that the S_{ARTS} calculations do not suffer from this ambiguity, since one can simply use the model at the prescribed p/T .

Table 4 also lists S values quoted for HITRAN 2016 in the supplement of Hodnebrog, Aamaas, et al. (2020), which we will refer to as Hod20 from now on. These are based on the same data set that we use so the numbers should be comparable. Indeed, discrepancies between S_{ARTS} and S_{Hod} are mostly below 1%. In a few cases they are around 2%–6%.

A possible issue affecting the S value is zeroing of negative laboratory absorption data, which is done in the default HITRAN data, but not in an alternative data version, also available from HITRAN. However, both this work and Hod20 use the default version (without negative values), ruling out that source of discrepancy.

In the case of the bigger discrepancies, the S_{Hod} value is lower (HFC134a, HFC152a, CH_3CCl_3 , CH_2Cl_2 , Halon1301). For Halon1301, the reason is the inconsistency of the HITRAN cross-section data at different temperatures, discussed above. For the rest of these species, the reason is the smaller frequency range used in Hod20 for the S calculation (compare ranges given in Tables 2 and 3 to those given in the Hod20 supplement). Limiting the S_{ARTS} calculation to the Hod20 frequency range for these species results in differences below 1%. It should be noted that these S differences due to integration frequency range do not directly affect radiative forcing, since the frequency ranges omitted in Hod20 are either so high that they contribute little to the forcing (far away from the peak of the Planck function for terrestrial temperatures), or, in the case of HFC134a, masked by the CO_2 band.

3. Forcing Estimates

The new absorption model was used to estimate instantaneous clear-sky REs and PD radiative forcing of the different trace gases considered. Radiative forcing is defined here as the reduction in upwelling broadband (spectrally integrated) longwave radiation when the concentration of the species is increased by some amount from a reference value, and is given in units of W m^{-2} . Radiative efficiency is the forcing divided by the concentration of the gas species, given in units of $\text{W m}^{-2} \text{ppb}^{-1}$. For gases with very small concentrations and thus small optical depths, as the ones considered here, the efficiency is a good measure of the strength of their radiative effect, since the impact on radiation is linear in concentration. (For more abundant gases the radiative effect behaves non-linearly, so this concept is not applicable.)

In the spirit of RFMIP (Pincus et al., 2016), we concentrate on the simple instantaneous clear-sky case. Instantaneous meaning that we do not apply a stratospheric adjustment, clear-sky meaning that we do not include clouds in the calculation. We also do not apply any corrections for the lifetime of the gas species. These corrections are discussed briefly in Hod20, and in more detail in Hodnebrog et al. (2013).

Forcing can be computed at different levels, in our case at the top of the atmosphere (TOA), at the TRP and at the SRF. For comparison with other studies quoting stratosphere-adjusted forcing, it should be noted that the adjustment will lower the TOA value and increase the TRP value, so that in the adjusted case these two are equal.

3.1. Atmospheric Scenarios and RT Model Setup

For RFMIP, a set of 100 atmospheres and corresponding averaging weights was developed in order to minimize sampling error in estimates of PD to pre-industrial (PI) forcing by all greenhouse gases, not only in the global mean

Table 3

Considered Cross-Section Species Together With Spectral, Pressure and Temperature Limits and With $O_{p,T}$ the Maximum Polynomial Order of the Pressure/Temperature Dependency of the Band. (Continuation of Previous Table)

Species	Band	$\tilde{\nu}_{\min}$ [cm^{-1}]	$\tilde{\nu}_{\max}$ [cm^{-1}]	$\delta\tilde{\nu}$ [cm^{-1}]	p_{\min} [hPa]	p_{\max} [hPa]	T_{\min} [K]	T_{\max} [K]	O_p	O_T
HFC4310mee	0	500	550	0.060	1013.25	1013.25	278.10	323.10	0	1
	1	550	3,500	0.030	0.00	1013.25	278.10	340.00	1	1
	2	3,500	6,500	0.060	1013.25	1013.25	278.10	323.10	0	1
CH3CCI3	0	500	6,500	0.060	1013.25	1013.25	278.10	323.10	0	1
CCI4	0	700	860	0.001	10.00	1013.25	207.90	296.70	1	2
CH2Cl2	0	600	6,500	0.060	1013.25	1013.25	278.10	323.10	0	1
CHCl3	0	580	725	0.060	1013.25	1013.25	278.10	323.10	0	1
	1	725	805	0.048	0.00	1013.25	253.00	323.10	1	1
	2	805	7,200	0.060	1013.25	1013.25	278.10	323.10	0	1
Halon1211	0	600	6,500	0.060	1013.25	1013.25	278.10	323.10	0	1
Halon1301	0	510	6,500	0.060	1013.25	1013.25	278.10	323.10	0	1
Halon2402	0	550	6,500	0.060	1013.25	1013.25	278.10	323.10	0	1
NF3	0	600	6,500	0.060	1013.25	1013.25	278.10	323.10	0	1
SF6	0	560	925	0.060	1013.25	1013.25	278.10	323.10	0	1
	1	925	955	0.005	26.93	1013.52	180.00	323.10	1	2
	2	955	6,500	0.060	1013.25	1013.25	278.10	323.10	0	1
SO2F2	0	500	6,500	0.060	1013.25	1013.25	278.10	323.10	0	1
CF4	0	570	1,250	0.060	1013.25	1013.25	278.10	323.10	0	1
	1	1,250	1,290	0.003	10.05	1014.58	180.40	323.10	1	2
	2	1,290	6,500	0.060	1013.25	1013.25	278.10	323.10	0	1
C2F6	0	500	680	0.060	1013.25	1013.25	278.10	323.10	0	1
	1	680	750	0.015	0.00	1013.25	253.00	323.10	1	1
	2	750	1,061	0.060	1013.25	1013.25	278.10	323.10	0	1
	3	1,061	1,165	0.003	0.00	1013.65	180.60	323.10	1	2
	4	1,165	1,170	0.060	1013.25	1013.25	278.10	323.10	0	1
	5	1,170	1,220	0.030	0.00	1013.25	253.00	323.10	1	1
	6	1,220	1,285	0.003	0.00	1013.65	180.60	323.10	1	2
	7	1,285	1,380	0.030	0.00	1013.25	253.00	323.10	1	1
	8	1,380	6,500	0.060	1013.25	1013.25	278.10	323.10	0	1
C3F8	0	600	6,500	0.060	1013.25	1013.25	278.10	323.10	0	1
cC4F8	0	550	555	0.061	1013.25	1013.25	278.10	323.10	0	1
	1	555	590	0.015	0.00	1013.25	253.00	323.10	1	1
	2	590	900	0.060	1013.25	1013.25	278.10	323.10	0	1
	3	900	1,460	0.015	0.00	1013.25	253.00	323.10	1	1
	4	1,460	6,500	0.060	1013.25	1013.25	278.10	323.10	0	1
C4F10	0	500	6,500	0.060	1013.25	1013.25	278.10	323.10	0	1
C5F12	0	500	700	0.060	1013.25	1013.25	278.10	323.10	0	0
	1	700	1,400	0.012	0.00	1013.25	278.10	323.10	0	1
	2	1,400	6,500	0.060	1013.25	1013.25	278.10	323.10	0	0
C6F14	0	700	1,400	0.012	0.00	0.00	297.00	297.00	0	0
C8F18	0	700	1,400	0.012	0.00	0.00	297.00	297.00	0	0

Table 4
Integrated Absorption Cross-Sections

Species	S_{HITRAN}	S_{ARTS}	S_{Hod}	$\Delta_{\text{ARTS-HITRAN}}$	$\Delta_{\text{ARTS-Hod}}$
	[$10^{-17} \text{ cm}^2 \text{ cm}^{-1}$]	[$10^{-17} \text{ cm}^2 \text{ cm}^{-1}$]	[$10^{-17} \text{ cm}^2 \text{ cm}^{-1}$]	[%]	[%]
CFC11	10.06	10.04	10.10	−0.22	−0.62
CFC12	13.51	13.59	13.50	0.57	0.64
CFC113	14.59	14.41	14.60	−1.20	−1.28
CFC114	17.39	17.40	17.40	0.07	−0.01
CFC115	12.10	12.09	12.10	−0.08	−0.09
HCFC22	10.48	10.52	10.50	0.35	0.15
HCFC141b	8.56	8.50	8.40	−0.69	1.24
HCFC142b	11.40	11.40	11.20	0.01	1.79
HFC23	12.28	12.28	12.30	−0.00	−0.14
HFC32	6.65	7.13	7.00	7.14	1.85
HFC125	17.53	17.69	17.40	0.94	1.68
HFC134a	14.11	14.02	13.20	−0.64	6.24
HFC143a	14.14	14.21	13.80	0.46	2.97
HFC152a	8.45	8.46	8.00	0.21	5.81
HFC227ea	25.40	25.16	25.30	−0.95	−0.54
HFC236fa	22.81	22.81	22.80	0.00	0.05
HFC245fa	19.57	19.57	19.60	0.00	−0.17
HFC365mfc	18.75	18.75	18.80	0.00	−0.29
HFC4310mee	30.51	30.81	30.40	1.00	1.36
CH3CCI3	5.53	5.52	5.30	−0.23	4.06
CCl4	6.73	6.54	6.70	−2.74	−2.33
CH2Cl2	2.95	2.95	2.80	0.02	5.43
CHCl3	5.02	5.06	5.00	0.70	1.19
Halon1211	13.24	13.30	13.20	0.50	0.79
Halon1301	16.09	16.90	16.10	4.99	4.94
Halon2402	16.14	16.20	16.10	0.38	0.63
NF3	7.23	7.26	7.20	0.43	0.86
SF6	20.93	21.18	21.20	1.23	−0.08
SO2F2	14.04	13.91	14.00	−0.93	−0.66
CF4	20.14	20.09	19.80	−0.27	1.46
C2F6	22.76	22.90	23.10	0.61	−0.87
C3F8	27.51	27.00	27.50	−1.83	−1.80
cC4F8	21.73	21.74	21.70	0.04	0.19
C4F10	32.45	32.43	32.40	−0.08	0.09
C5F12	37.34	37.61	37.30	0.72	0.83
C6F14	38.54	38.54	38.50	0.00	0.11
C8F18	45.55	45.55	45.60	0.00	−0.10

Note. The S columns are integrated absorption cross-sections for HITRAN, the new ARTS model, and Hod20. The latter are the values given in the appendix for the database “H16” (HITRAN 2016) so they should be based on exactly the same data as ours. For a few species, where there is no “H16” value in Hod20, another suitable entry is used. These are documented in the footnotes of Table 5. The last two columns show percentage differences relative to HITRAN and Hod20.

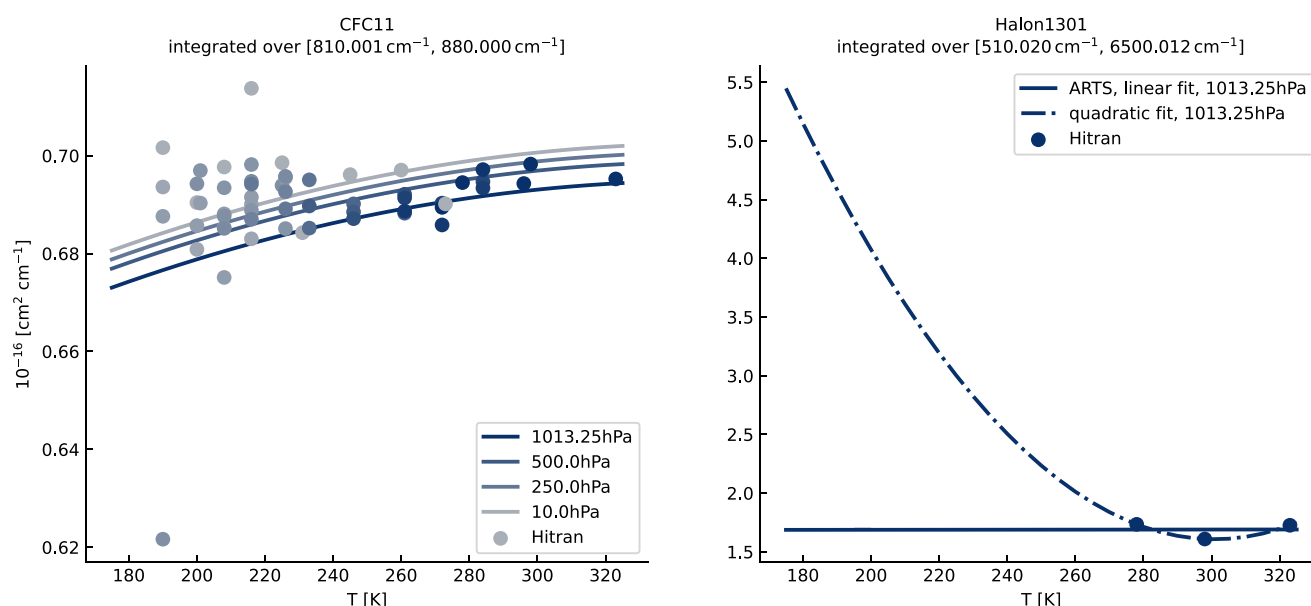


Figure 3. Integrated absorption cross-sections S as a function of temperature for CFC11 and Halon1301. Lines denote fitted absorption cross-sections, circles denote HITRAN observations, color shading indicates pressure. For Halon1301 the integrated absorption cross-section when using a quadratic fit instead of a linear fit is also shown. Note that we do not use the quadratic fit, it is merely meant to illustrate the danger of overfitting.

at the TOA but regionally and at various levels in the atmosphere (Pincus et al., 2020). The same set of atmospheres and weights was used here. The standard error from the averaging can be used as a conservative estimate of the deviation of this mean value from the true global mean, which is found to be always below approximately 5%. Simulations were done for the scenarios “PD” and “preindustrial” of RFMIP/CMIP (Meinshausen et al., 2017; Pincus et al., 2016). Atmospheric conditions are given at 61 pressure levels from the SRF to 0.01 Pa. With a few exceptions (CCl_4 , CH_3Cl , CH_2Cl_2 , CHCl_3 , CH_3Br , CF_4), halocarbon concentrations are zero in the preindustrial scenario. Of the absorbing species concentrations, only H_2O and O_3 are specified as functions of pressure level. All other gases, including all halocarbons, are assumed to be well-mixed. For information on other included absorbing gas species beside halocarbons see list at the end of this section. Halocarbon concentrations can be found in Table 6.

The ARTS model (version 2.5, (Buehler et al., 2005, 2018; Eriksson et al., 2011)) was used for the forcing and radiative efficiency estimates. As outlined in Section 1, we calculate the forcing by doing one reference simulation of radiation fluxes and then, for each gas, one simulation where that gas is removed. This was done for all 100 atmospheres, then averaged with the correct RFMIP weights.

Fluxes were calculated using Gauss–Legendre quadrature with three radiation streams per hemisphere and with a frequency resolution of 0.05 cm^{-1} (64,801 individual frequencies in the interval $10\text{--}3,250 \text{ cm}^{-1}$). We evaluate them at the SRF, at the TOA, and at the TRP, using the World Meteorological Organization definition for the latter.

Absorbing species were modeled either from spectral line data or with the new polynomial model based on the HITRAN laboratory cross-section. Spectral line species were H_2O , O_2 , O_3 , N_2 , CO , CO_2 , CH_4 , N_2O , CH_3Br , and CH_3Cl . Additionally, MT_CKD version 2.5.2 absorption continua (Mlawer et al., 2012) were included for H_2O , N_2 and CO_2 (but no CO_2 line mixing), and the MT_CKD version 1.0 continuum was included for O_2 .

3.2. Radiative Efficiencies

Figure 4a shows instantaneous clear-sky REs at the TOA. The blue bars mark a calculation where the spectrum at the fixed surface temperature and surface pressure is used throughout the atmosphere, as in earlier assessments (Hodnebrog, Aamaas, et al., 2020, and references therein). Where the available data allow it, we have parameterized the T dependence (red bars) or the T and p dependence (orange bars), as described above. Figure 4b shows the relative difference of the other bars from the blue bars.

Table 5
Instantaneous Radiative Efficiencies in Units of $\text{Wm}^{-2} \text{ppb}^{-1}$

Species	Clear TOA	Clear TRP	All-sky TRP	Hod.	Diff. Hod.
Chlorofluorocarbons					
CFC11	0.408	0.354	0.265	0.263	−1%
CFC12	0.493	0.423	0.317	0.299	−6%
CFC113	0.475	0.422	0.316	0.301	−5%
CFC114	0.443	0.399	0.299	0.310	4%
CFC115 ^a	0.310	0.267	0.200	0.186	−7%
Hydrochlorofluorocarbons					
HCFC22	0.321	0.280	0.210	0.201	−4%
HCFC141b	0.242	0.217	0.162	0.158	−3%
HCFC142b	0.287	0.246	0.184	0.179	−3%
Hydrofluorocarbons					
HFC23	0.303	0.259	0.194	0.180	−7%
HFC32	0.165	0.147	0.110	0.115	4%
HFC125	0.367	0.313	0.234	0.220	−6%
HFC134a	0.262	0.226	0.169	0.157	−7%
HFC143a	0.262	0.222	0.167	0.157	−6%
HFC152a	0.188	0.162	0.122	0.115	−6%
HFC227ea	0.409	0.352	0.264	0.256	−3%
HFC236fa ^b	0.375	0.319	0.240	0.223	−7%
HFC245fa ^c	0.376	0.328	0.246	0.228	−7%
HFC365mfc ^d	0.356	0.304	0.228	0.213	−7%
HFC4310mee	0.512	0.446	0.335	0.330	−1%
Chlorocarbons and hydrochlorocarbons					
CH ₃ CCl ₃	0.088	0.088	0.066	0.069	5%
CCl ₄	0.249	0.222	0.167	0.174	4%
CH ₃ Cl ^e	0.008	0.008	0.006	0.006	−1%
CH ₂ Cl ₂	0.065	0.061	0.046	0.047	2%
CHCl ₃	0.187	0.167	0.126	0.121	−4%
Bromocarbons, hydrobromocarbons and halons					
CH ₃ Br ^f	0.006	0.005	0.004	0.006	57%
Halon1211	0.477	0.410	0.308	0.293	−5%
Halon1301	0.471	0.405	0.303	0.269	−11%
Halon2402	0.477	0.426	0.320	0.305	−5%
Fully fluorinated species					
NF ₃	0.300	0.260	0.195	0.189	−3%
SF ₆	0.838	0.715	0.536	0.518	−3%
SO ₂ F ₂	0.309	0.272	0.204	0.207	2%
CF ₄	0.137	0.122	0.092	0.092	0%
C ₂ F ₆	0.381	0.328	0.246	0.240	−3%
C ₃ F ₈	0.347	0.326	0.245	0.253	3%
cC ₄ F ₈	0.472	0.403	0.303	0.279	−8%
C ₄ F ₁₀	0.528	0.458	0.344	0.337	−2%

As the figure shows, the p/T dependence leads to differences of up to approximately 8% in some cases. But in most cases the error is much less than this. Inspection of the plots similar to Figure 3 (included with the data distribution) reveals that in all cases where Figure 4 indicates a strong temperature dependence (CFC113, CFC114, HFC32, HFC4310mee, C3F8), there is a temperature dependence in the frequency integrated absorption cross-section S . This indicates that it is this change in integrated value that affects radiative efficiency, not the temperature dependence at individual frequencies. As discussed in Section 2.3, a strong temperature dependence of S is not physically plausible, but rather reflects the uncertainty in the laboratory data, so overall this analysis confirms the validity of the traditional approach to ignore the temperature (and pressure) dependence when estimating REs.

Table 5 summarizes all REs calculated with our model. Compared to Figure 4, it includes two additional molecular species for completeness, CH₃Br and CH₃Cl, which we have calculated from spectral line data, not with the cross-section model.

Our focus is on the new halocarbon absorption model, not on providing the most realistic estimate or the most climatically relevant radiative efficiency. We therefore focus on the instantaneous clear-sky forcing, ignoring stratospheric adjustment and clouds. The table gives this in the first two columns, at the TOA and at the TRP. For the sake of comparison with Hod20 we also make a very rough estimate of the all-sky value at the TRP by simply multiplying the clear-sky value with 0.75, the ratio between instantaneous values at the TRP with and without clouds that Myhre et al. (2006) find for CFC12. This value is also consistent with the range of clear-sky to all-sky conversion factors in Table 3 of Pincus et al. (2020). Note that in reality this factor will vary somewhat from species to species, which could be responsible for some of the differences to the Hod20 values in Table 5.

We can compare the new RE values with those given in the electronic supplement of Hod20, focusing on the values for HITRAN 2016, the database we use. Of the given forcing quantities, the Hod20 value for the new instantaneous RE is most comparable to our all-sky TRP value. Table 5 therefore lists these values for comparison, as well as their relative difference to ours.

It is important to note that Hodnebrog et al. use the Pinnock method, using only halocarbon spectra at surface pressure and ambient temperature, whereas we parameterize the absorption dependence in p/T space where possible, as discussed above.

On average, our values are 1.6% higher than those of Hod20, but there is one species, CH₃Br, for which our value is 57% lower. This is one of the two species for which HITRAN absorption cross-sections are not available and that we have therefore calculated from spectral line data. Normally one would trust the explicit spectral line calculation more than the cross-sections, but in this case examination of the catalog reveals that the HITRAN line parameter list for CH₃Br is incomplete. The relevant band at 600 cm^{−1} is missing completely, as can also be seen in Figure 2 of Kochanov et al. (2015). HITRAN plans to complete these data in the near future.

This problem only affects CH₃Br, and agreement is much better, 1%, for CH₃Cl, the other species that we have computed from spectral line data. When ignoring the outlier CH₃Br, our values are on average approximately 3% higher than those of Hod20. Again with the exception of CH₃Br, all

Table 5
Continued

Species	Clear TOA	Clear TRP	All-sky TRP	Hod.	Diff. Hod.
C5F12	0.580	0.509	0.381	0.370	−3%
C6F14 ^a	0.656	0.568	0.426	0.407	−5%
C8F18 ^b	0.760	0.660	0.495	0.471	−5%
Mean difference					−1.6%

Note. The first four numerical columns contain the clear-sky value at the top of the atmosphere (“clear TOA”), the clear-sky value at the tropopause (“clear TRP”), the all sky value at the tropopause (“all-sky TRP”, simply estimated as 0.75 times the clear TRP value), and the corresponding value given in the Appendix of Hod20 as “New inst. RE” for the H16 (HITRAN 2016) database (“Hod.”). The last column contains the relative difference of the Hod20 value to our “all-sky TRP” value.

^aHod20 value is from row labeled “H08”, based on same laboratory data. ^bHod20 value is from row labeled “Sihra et al. (2001),” based on same laboratory data. ^cHod20 value is from row labeled “Sihra et al. (2001),” based on same laboratory data. ^dHod20 value is from row labeled “Inoue et al. (2008),” based on same laboratory data. ^eOur value is based on explicit spectral line calculations, Hod20 value is from row labeled “Wallington et al. (2016).” ^fOur value is based on explicit spectral line calculations, Hod20 value is from row labeled “Pacific Northwest National Laboratory.” Note that the HITRAN line data in this case are incomplete, as discussed in the text. ^gHod20 value is from row labeled “Bravo et al. (2010),” based on same laboratory data. ^hHod20 value is from row labeled “Bravo et al. (2010),” based on same laboratory data.

differences are below approximately 10%. We consider this level of agreement as very good given the differences in methodology.

The most obvious factors contributing to the differences for individual species are (a) different integrated halocarbon absorption coefficient S , (b) the missing temperature dependence in the Hod20 calculations, (c) the atmospheric states (100 RFMIP profiles vs. 2 profiles), (d) our crude clear-sky to all sky correction and (e) the TRP definition used.

From Table 4 and the accompanying discussion, we conclude that factor a should not play a significant role except for the few cases where HITRAN data at different temperatures are most inconsistent (HFC32, CCl₄, Halon1301), where it could contribute a few percent. From Figure 4 and the accompanying discussion we conclude that factor b can also contribute a few percent to the difference, in particular for CFC114 and HFC4310mee. A similar contribution from the remaining factors c–e is plausible. There also likely is significant cancellation of errors, as the factors are uncorrelated.

3.3. Present Day Forcing

Table 6 shows the PD instantaneous clear-sky radiative forcings of the different species investigated. As Table 5, it includes CH₃Br and CH₃Cl for completeness, calculated from spectral line data, not with the cross-section model. Note that this is the PD scenario of RFMIP, with a CO₂ concentration representative of the year 2014.

The main value of these data is that they break down the instantaneous clear-sky forcing, as presented in Pincus et al. (2020), by halocarbon component.

Units and computation setup are identical, so that the numbers can be directly compared. We also provide an improved estimate of the total halocarbon forcing in that framework.

Before turning to that, we can also roughly compare our results to earlier halocarbon assessments, notably Hod20. Our PD forcing values are higher than those given in Table 4 of Hod20 but the numbers cannot be compared directly, since theirs are all-sky, include stratospheric adjustment, and include a lifetime correction. Of these three factors the first and third act to reduce their value, whereas the second acts to increase it.

Despite these differences, the ranking of forcing strength of the different species is remarkably consistent. The most significant difference in ranking is that in our calculation HFC125 has a weaker forcing than HFC23, whereas in theirs it is stronger. The reason for this difference is the assumed concentration of HFC125, which in the RFMIP/CMIP atmospheres that we used is only half of what is assumed in Hod20.

To put these results in perspective, Table 7 shows the corresponding forcings of the major greenhouse components, calculated by our model, using the same 100 RFMIP atmospheres and weights. Methodology is different here: Instead of leave-one-out calculations, the concentration profile of the component in question is replaced by its PI values. This is necessary because the optical depth of these components is substantial, making forcing a non-linear function of concentration.

The last entry in Table 7 gives the forcing from a simulation where all halocarbons are replaced by their PI concentrations. The close agreement of this number with the sum-total of the leave-one-out halocarbon simulations (last entry in Table 6) confirms that nonlinearities are not an issue for the halocarbons.

For the major atmospheric absorbers, results in Table 7 are in excellent agreement with the results presented in Pincus et al. (2020), Table 2. Those are average numbers across the participating benchmark models, where our model ARTS was one of six, but using an earlier halocarbon absorption model based on the convolution method (compare Section 2.2).

It is interesting to look at the level of agreement between our calculation here and the six benchmark model mean in Pincus et al. (2020). For the PD instantaneous clear-sky longwave forcing at the TOA, the differences (ARTS minus multi-model mean) are CO₂: −0.2%, CH₄: −0.8%, N₂O: −1.0%, O₃: −1.6%, halocarbons: +7.3%.

Table 6
Present-Day Instantaneous Clear-Sky Radiative Forcing by Halocarbons

Species	PI conc. [ppt]	PD conc. [ppt]	TOA [mW m^{-2}]	TRP [mW m^{-2}]	SRF [mW m^{-2}]
Chlorofluorocarbons					
CFC11	0.000	233.080	95.094	82.508	67.669
CFC12	0.000	520.581	256.590	220.217	186.051
CFC113	0.000	72.711	34.564	30.684	24.012
CFC114	0.000	16.307	7.226	6.511	5.240
CFC115	0.000	8.429	2.609	2.250	1.637
Hydrochlorofluorocarbons					
HCFC22	0.000	229.542	73.640	64.262	50.427
HCFC141b	0.000	23.809	5.766	5.157	3.600
HCFC142b	0.000	22.076	6.346	5.421	4.292
Hydrofluorocarbons					
HFC23	0.000	26.890	8.142	6.961	5.229
HFC32	0.000	8.337	1.372	1.226	1.021
HFC125	0.000	15.355	5.628	4.800	3.031
HFC134a	0.000	80.516	21.055	18.166	12.339
HFC143a	0.000	15.253	3.994	3.388	2.091
HFC152a	0.000	7.733	1.451	1.255	0.996
HFC227ea	0.000	1.006	0.411	0.354	0.218
HFC236fa	0.000	0.131	0.049	0.042	0.025
HFC245fa	0.000	2.047	0.770	0.671	0.465
HFC365mfc	0.000	0.765	0.272	0.233	0.153
HFC4310mee	0.000	0.247	0.126	0.110	0.069
Chlorocarbons and Hydrochlorocarbons					
CH ₃ CCl ₃	0.000	3.680	0.325	0.323	0.176
CCl ₄	0.025	83.070	20.699	18.461	10.819
CH ₃ Cl	457.000	539.542	0.210	0.293	0.024
CH ₂ Cl ₂	6.913	36.348	1.879	1.777	0.858
CHCl ₃	6.000	9.902	0.704	0.632	0.382
Bromocarbons, Hydrobromocarbons and Halons					
CH ₃ Br	5.300	6.686	0.007	0.006	0.004
Halon1211	0.004	3.754	1.787	1.538	1.278
Halon1301	0.000	3.298	1.552	1.334	0.996
Halon2402	0.000	0.431	0.206	0.184	0.132
Fully Fluorinated Species					
NF ₃	0.000	1.240	0.372	0.322	0.281
SF ₆	0.000	8.221	6.886	5.877	4.999
SO ₂ F ₂	0.000	2.039	0.630	0.554	0.402
CF ₄	34.050	81.092	5.458	4.981	1.041
C ₂ F ₆	0.000	4.399	1.674	1.444	0.823
C ₃ F ₈	0.000	0.601	0.208	0.196	0.120
cC ₄ F ₈	0.000	1.339	0.632	0.540	0.378
C ₄ F ₁₀	0.000	0.179	0.095	0.082	0.048
C ₅ F ₁₂	0.000	0.126	0.073	0.064	0.036

Table 6
Continued

Species	PI conc. [ppt]	PD conc. [ppt]	TOA [mW m^{-2}]	TRP [mW m^{-2}]	SRF [mW m^{-2}]
C6F14	0.000	0.279	0.183	0.159	0.087
C8F18	0.000	0.091	0.069	0.060	0.032
Sum total	—	—	568.755	493.041	391.479

Note. Columns 2 and 3 give the pre-industrial (PI) and present-day (PD) concentration, respectively. Remaining columns give the instantaneous clear-sky forcing (difference between PD and PI net fluxes) at the top of the atmosphere (TOA), tropopause (TRP) and at the surface (SRF). Values are calculated from the difference in the radiative effect of the species in the PD and the PI case. The last row gives the sum of all individual forcings. Comparison with the last row of Table 7 shows that the impact of nonlinearity for the halocarbons is very small.

So, indeed, the only major difference is in the halocarbons, confirming that it was worthwhile to investigate them more closely. Since our treatment of halocarbons is more elaborate and up to date than in the other RFMIP models, we interpret the approximately 7% difference to mean that at least some of the other RFMIP models presently underestimate the halocarbon forcing. This may be due to different representations of concentration change (all gases individually vs. using equivalent concentrations), or due to some models not having implemented all of the halocarbon species in the case of the explicit treatment.

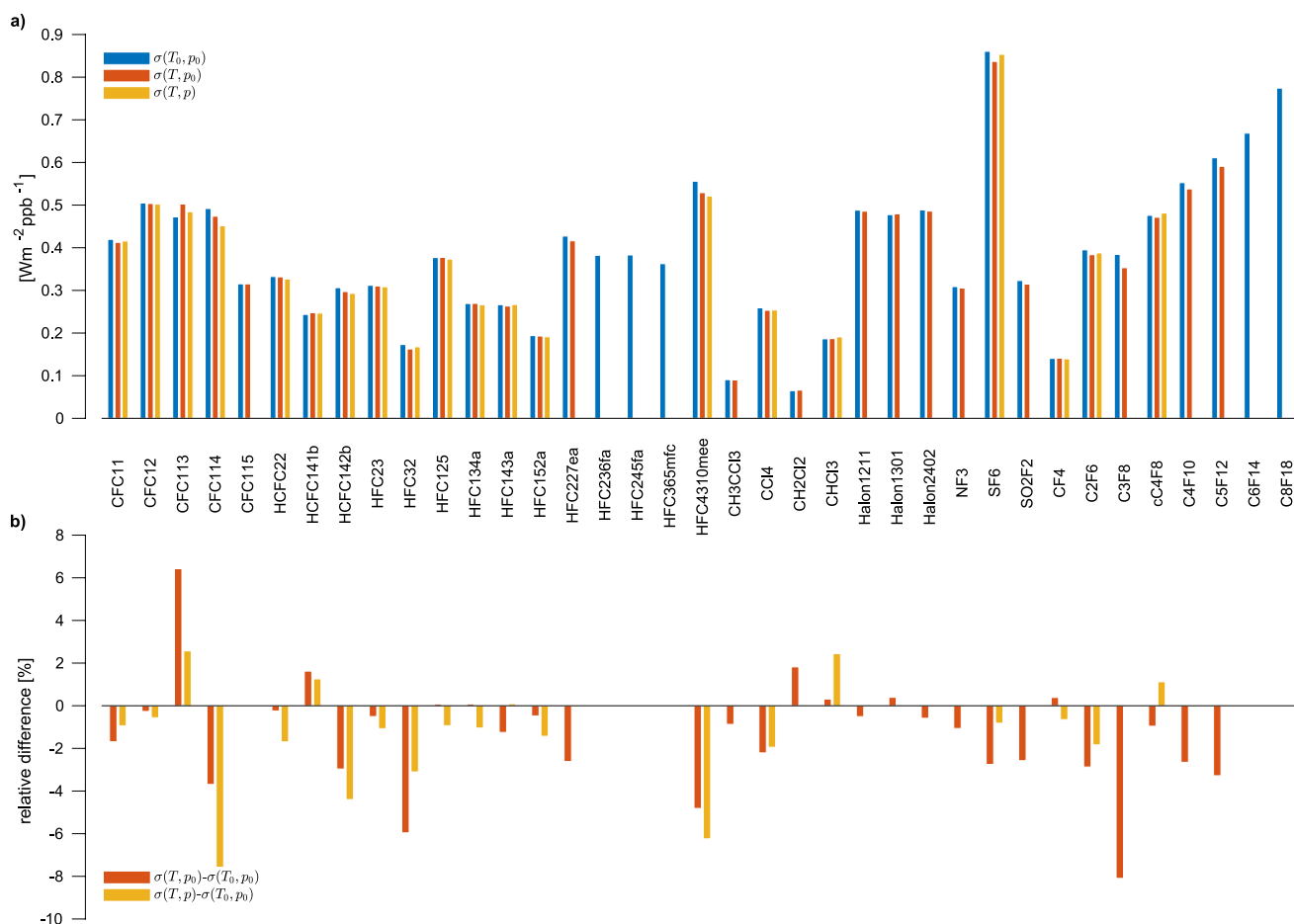


Figure 4. Radiative efficiency at the top of the atmosphere, comparing our default model with temperature and pressure dependence $\sigma(T, p)$ to simplified models with only temperature dependence $\sigma(T, p_0)$ or no dependence at all $\sigma(T_0, p_0)$. The values of the default parameters are $T_0 = 293$ K and $p_0 = 1,013$ hPa, so the last case corresponds to other studies such as Hod20 that just use the laboratory spectra at ambient temperature and surface pressure. The available laboratory data do not always allow the temperature fit, and even more rarely the pressure fit. This can be seen from the available bar colors in the top figure (and also from Table 2). In those cases our model does not include those dependencies.

Table 7
Major Components of Present-Day Instantaneous Clear-Sky Radiative Forcing

Species	PI conc. [ppm]	PD conc. [ppm]	TOA [Wm ⁻²]	TRP [Wm ⁻²]	SRF [Wm ⁻²]
Total	—	—	2.877	4.277	2.023
CO ₂	284	397	1.306	2.425	0.913
CH ₄	0.808	1.831	0.608	0.663	0.272
N ₂ O	0.273	0.327	0.203	0.224	0.0850
O ₃	1.901	1.813	0.127	0.403	0.316
Halocarbons	—	—	0.573	0.496	0.394

Note. Columns 2 and 3 give the pre-industrial (PI) and present-day (PD) concentration, respectively. Remaining columns give the instantaneous clear-sky forcing (difference between PD and PI net fluxes) at the top of the atmosphere (TOA), tropopause (TRP) and at the surface (SRF). Values are calculated from the difference between the present-day reference case and an atmosphere where the respective concentration has been replaced by its preindustrial value. Note in particular that for the halocarbons all their concentrations are changed at the same time. Also, total is the effect of changing all species concentrations at once from PD to PI, not the sum of the individual forcings. This table can be compared directly to the middle block of Table 2 in Pincus et al. (2020). For O₃, the concentration depends on location and altitude; the given concentration values are air density-weighted vertical means of the volume mixing ratio, weight-averaged over the 100 atmospheric cases.

Overall, halocarbons are responsible for a substantial share of the PD forcing, 0.573 Wm⁻² (instantaneous clear-sky at the TOA), corresponding to approximately 20% of the total anthropogenic forcing, or 44% compared to anthropogenic CO₂ forcing alone.

4. Summary and Conclusions

A new and simple model of halocarbon absorption has been developed. It is constructed by applying second order polynomial fits in pressure and temperature to HITRAN absorption cross-section data. The model reduces to the case without pressure and/or temperature dependence for gas species where data coverage is inadequate to do a fit.

The model was implemented and tested in ARTS, but was intentionally constructed so that it is very easy to use stand-alone or in other radiative transfer models: Polynomial coefficients are stored in data files, and the formula to apply them is given in this article, in the ARTS source code, and in stand-alone Python code (see Section 5).

Currently, the model is implemented for 37 of the 40 halocarbon species requested by RFMIP/CMIP (we model CH₃Cl and CH₃Br explicitly from spectral line data and completely omit C₇F₁₆, for which HITRAN has no data). It could easily be extended to other gases, to the extent that cross-section data are available.

The model improves on previously available options for using spectral cross-sections, which were to use the cross-section data for particular pressure/temperature conditions directly (ignoring the dependencies),

as in Hod20, to do an explicit (temperature) interpolation of the cross-section data inside the RT code, as in MODTRAN (Berk et al., 2005), to use an algorithmic model with looser connection to the cross-section data, as in LBLRTM (Clough et al., 2005), or to use a pseudo-line list available only for selected species, as in SFIT (Hase et al., 2004). In particular, in our approach it is completely transparent how the model is constructed from the data, all species are treated consistently, and the available data are fully exploited.

Such a model has many applications, for example, in remote sensing, in generating *k*-distributions for circulation model radiation schemes, and in calculating radiative energy fluxes. In the last of these areas we presented an application in this article, namely the estimation of radiative efficiency and PD radiative forcing of the different halocarbon species. Results for radiative efficiency are broadly consistent with the recent assessment by Hod20, within approximately 10%. A larger discrepancy for one species (57% for CH₃Br) that we have modeled from explicit spectroscopic line parameters, not the new absorption model, was found to be due to incomplete HITRAN line data.

For the other gas species, part of the differences can be explained by slightly different values of the integrated absorption band strength *S* due to inconsistencies of HITRAN data at different temperature. Remaining differences are likely due to the crude cloud correction that we have done for the sake of comparison to the Hod20 all-sky values, and due to the different assumed atmospheric states (100 RFMIP atmospheres vs. 2 Hod20 atmospheres).

An added value of our new analysis is that we quantify the impact of the temperature dependence for all gas species where the laboratory data allow it. We find the difference in radiative efficiency to be significant—in some cases, up to approximately 8%. However, the differences appear to be due to inconsistencies in the integrated absorption cross-section *S* in laboratory data at different temperatures, rather than due to the temperature dependence at individual frequencies per se. This is especially notable for Halon1301, for which we forgo a quadratic temperature fit, because it would lead to an unacceptably large temperature dependence in *S*.

Overall, this stresses the need for more laboratory measurements, especially at low temperatures. Data at different temperatures are not informative if the temperature range is narrow relative to the range of temperatures in the atmosphere: Data down to 280 K, as for Halon1301 are not enough, they should reach down to below 200 K, as

for CFC11. It also stresses the need for fitting exercises such as ours in order to test the consistency of the laboratory data across the different temperatures and pressures.

Our direct simulations with the new halocarbon absorption model confirm the substantial PD radiative forcing by halocarbons that was already reported by earlier assessments. Although the effect is spread over many different compounds, and the contribution of each individual compound is relatively small, three compounds stick out: The largest individual contributions are by CFC12 (257 mW m⁻² instantaneous clear-sky forcing at the TOA), CFC11 (95 mW m⁻²) and HCFC22 (74 mW m⁻²). Together, these three compounds are responsible for almost 75% of the sum-total of the halocarbon forcings. This emphasizes the critical importance of monitoring the decline of these substances in response to the Montreal Protocol. For CFC11, in particular, the decline slowed after 2013 (see Chen et al., 2020, and references therein). Fortunately, newer studies indicate an again faster decline from 2019 on (Montzka et al., 2021; Park et al., 2021).

Data Availability Statement

The absorption model coefficients are published in NetCDF format on Zenodo (<https://zenodo.org/record/6542792>). These coefficients are generated with the ARTS-crossfit software package which is available on Github (<https://github.com/atmtools/arts-crossfit/releases/tag/v1.0.0>). For reproducibility, the version of ARTS that was used for the calculations in this article can be retrieved from Github (<https://github.com/atmtools/arts/tree/c0cc180d>). For other calculations, the use of version 2.5.4 or later (<https://github.com/atmtools/arts/releases>) is recommended since the ARTS model is continuously developed and improved.

Acknowledgments

An earlier version of the new absorption model was evaluated and compared against LBLRTM by Hanna Dunke in the context of her bachelor's thesis. We thank Eli Mlawer for providing the LBLRTM results for that exercise. We also thank two anonymous reviewers, and in particular editor Keith Shine, for extensive and constructive comments and suggestions, which helped us substantially improve the manuscript. Furthermore, we would like to acknowledge the general support from the ARTS developer and user community. This work contributes to the Cluster of Excellence Climate, Climatic Change, and Society (CLICCS) and to the Center for Earth System Research and Sustainability (CEN) of Universität Hamburg. It was also partly supported by the US National Oceanic and Atmospheric Administration under award NA20AR4310375. Open Access funding enabled and organized by Projekt DEAL.

References

- Bak, J., Liu, X., Birk, M., Wagner, G., Gordon, I. E., & Chance, K. (2020). Impact of using a new ultraviolet ozone absorption cross-section dataset on OMI ozone profile retrievals. *Atmospheric Measurement Techniques*, 13(11), 5845–5854. <https://doi.org/10.5194/amt-13-5845-2020>
- Berk, A., Anderson, G. P., Acharya, P. K., Bernstein, L. S., Muratov, L., Lee, J., et al. (2005). MODTRAN5: A reformulated atmospheric band model with auxiliary species and practical multiple scattering options. In A. M. Larar, M. Suzuki, & Q. Tong (Eds.), *Multispectral and hyperspectral remote sensing instruments and applications II* (Vol. 5655, pp. 88–95). SPIE. <https://doi.org/10.1117/12.578758>
- Bravo, I., Aranda, A., Hurley, M. D., Marston, G., Nutt, D. R., Shine, K. P., et al. (2010). Infrared absorption spectra, radiative efficiencies, and global warming potentials of perfluorocarbons: Comparison between experiment and theory. *Journal of Geophysical Research*, 115, D24317. <https://doi.org/10.1029/2010JD014771>
- Buehler, S. A., Eriksson, P., Kuhn, T., von Engel, A., & Verdes, C. (2005). ARTS, the atmospheric radiative transfer simulator. *Journal of Quantitative Spectroscopy & Radiative Transfer*, 91(1), 65–93. <https://doi.org/10.1016/j.jqsrt.2004.05.051>
- Buehler, S. A., Mendrok, J., Eriksson, P., Perrin, A., Larsson, R., & Lemke, O. (2018). ARTS, the atmospheric radiative transfer simulator—Version 2.2, the planetary toolbox edition. *Geoscientific Model Development*, 11(4), 1537–1556. <https://doi.org/10.5194/gmd-11-1537-2018>
- Chen, X., Huang, X., & Strow, L. L. (2020). Near-global CFC-11 trends as observed by atmospheric infrared sounder from 2003 to 2018. *Journal of Geophysical Research: Atmosphere*, 125(22), 1–14. <https://doi.org/10.1029/2020JD033051>
- Clough, S. A., Shephard, M. W., Mlawer, E. J., Delamere, J. S., Iacono, M., Cady-Pereira, K., et al. (2005). Atmospheric radiative transfer modeling: A summary of the AER codes. *Journal of Quantitative Spectroscopy & Radiative Transfer*, 91(2), 233–244. <https://doi.org/10.1016/j.jqsrt.2004.05.058>
- Eriksson, P., Buehler, S. A., Davis, C. P., Emde, C., & Lemke, O. (2011). ARTS, the atmospheric radiative transfer simulator, version 2. *Journal of Quantitative Spectroscopy & Radiative Transfer*, 112(10), 1551–1558. <https://doi.org/10.1016/j.jqsrt.2011.03.001>
- Eyring, V., Bony, S., Meehl, G. A., Senior, C. A., Stevens, B., Stouffer, R. J., & Taylor, K. E. (2016). Overview of the coupled model inter-comparison project phase 6 (CMIP6) experimental design and organization. *Geoscientific Model Development*, 9(5), 1937–1958. <https://doi.org/10.5194/gmd-9-1937-2016>
- Gordon, I. E., Rothman, L. S., Hargreaves, R. J., Hashemi, R., Karlovets, E. V., Skinner, F. M., et al. (2022). The HITRAN2020 molecular spectroscopic database. *Journal of Quantitative Spectroscopy & Radiative Transfer*, 277, 107949.
- Gordon, I. E., Rothman, L. S., Hill, C., Kochanov, R. V., Tan, Y., Bernath, P. F., et al. (2017). The HITRAN2016 molecular spectroscopic database. *Journal of Quantitative Spectroscopy & Radiative Transfer*, 203, 1–66. <https://doi.org/10.1016/j.jqsrt.2017.06.038>
- Harrison, J. J. (2018). New and improved infrared absorption cross sections for trichlorofluoromethane (CFC-11). *Atmospheric Measurement Techniques*, 11(10), 5827–5836. <https://doi.org/10.5194/amt-11-5827-2018>
- Hase, F., Hannigan, J. W., Coffey, M. T., Goldman, A., Höpfner, M., Jones, N. B., et al. (2004). Intercomparison of retrieval codes used for the analysis of high-resolution, ground-based FTIR measurements. *Journal of Quantitative Spectroscopy & Radiative Transfer*, 87(1), 25–52. <https://doi.org/10.1016/j.jqsrt.2003.12.008>
- Hodnebrog, Ø., Aamaas, B., Fuglestad, J. S., Marston, G., Myhre, G., Nielsen, C. J., et al. (2020a). Updated global warming potentials and radiative efficiencies of halocarbons and other weak atmospheric absorbers. *Reviews of Geophysics*, 58(3), 1–30. <https://doi.org/10.1029/2019RG000691>
- Hodnebrog, Ø., Etminan, M., Fuglestad, J. S., Marston, G., Myhre, G., Nielsen, C. J., et al. (2013). Global warming potentials and radiative efficiencies of halocarbons and related compounds: A comprehensive review. *Reviews of Geophysics*, 51(2), 300–378. <https://doi.org/10.1002/rog.20013>
- Hodnebrog, Ø., Myhre, G., Kramer, R. J., Shine, K. P., Andrews, T., Faluvegi, G., et al. (2020). The effect of rapid adjustments to halocarbons and N₂O on radiative forcing. *Npj Climate and Atmospheric Science*, 3(43), 43. <https://doi.org/10.1038/s41612-020-00150-x>
- Huang, Y., Tan, X., & Xia, Y. (2016). Inhomogeneous radiative forcing of homogeneous greenhouse gases. *Journal of Geophysical Research: Atmosphere*, 121(6), 2780–2789. <https://doi.org/10.1002/2015JD024569>

- Inoue, Y., Kawasaki, M., Wallington, T. J., & Hurley, M. D. (2008). Atmospheric chemistry of $\text{CF}_3\text{CH}_2\text{CF}_2\text{CH}_3$ (HFC-365mfc): Kinetics and mechanism of chlorine atom initiated oxidation, infrared spectrum, and global warming potential. *Chemical Physics Letters*, 462(4–6), 164–168. <https://doi.org/10.1016/j.cplett.2008.07.054>
- Jacquinet-Husson, N., Armante, R., Scott, N., Chédin, A., Crépeau, L., Boutammine, C., et al. (2016). The 2015 edition of the GEISA spectroscopic database. *Journal of Molecular Structure*, 327, 31–72. New Visions of Spectroscopic Databases, Volume II. <https://doi.org/10.1016/j.jms.2016.06.007>
- Johnson, T. J., Profeta, L. T. M., Sams, R. L., Griffith, D. W. T., & Yokelson, R. L. (2010). An infrared spectral database for detection of gases emitted by biomass burning. *Vibrational Spectroscopy*, 53(1), 97–102. <https://doi.org/10.1016/j.vibspec.2010.02.010>
- Kochanov, R. V., Gordon, I. E., Rothman, L. S., Sharpe, S. W., Johnson, T. J., & Sams, R. L. (2015). Comment on “radiative forcings for 28 potential Archean greenhouse gases” by Byrne and Goldblatt. *Climate of the Past*, 11(8), 1097–1105. <https://doi.org/10.5194/cp-11-1097-2015>
- Kochanov, R. V., Gordon, I. E., Rothman, L. S., Shine, K. P., Sharpe, S. W., Johnson, T. J., et al. (2019). Infrared absorption cross-sections in HITRAN 2016 and beyond: Expansion for climate, environment, and atmospheric applications. *Journal of Quantitative Spectroscopy & Radiative Transfer*, 230, 172–221. <https://doi.org/10.1016/j.jqsrt.2019.04.001>
- Meinshausen, M., Vogel, E., Nauels, A., Lorbacher, K., Meinshausen, N., Etheridge, D. M., et al. (2017). Historical greenhouse gas concentrations for climate modelling (CMIP6). *Geoscientific Model Development*, 10(5), 2057–2116. <https://doi.org/10.5194/gmd-10-2057-2017>
- Mlawer, E. J., Payne, V. H., Moncet, J.-L., Delamere, J. S., Alvarado, M. J., & Tobin, D. C. (2012). Development and recent evaluation of the MT_CKD model of continuum absorption. *Philosophical Transactions of the Royal Society A*, 370(1968), 2520–2556. <https://doi.org/10.1098/rsta.2011.0295>
- Montzka, S. A., Dutton, G. S., Portmann, R. W., Chipperfield, M. P., Davis, S., Feng, W., et al. (2021). A decline in global CFC-11 emissions during 2018–2019. *Nature*, 590(7846), 428–432. <https://doi.org/10.1038/s41586-021-03260-5>
- Myhre, G., Stordal, F., Gausemei, I., Nielsen, C. J., & Mahieu, E. (2006). Line-by-line calculations of thermal infrared radiation representative for global condition: CFC-12 as an example. *Journal of Quantitative Spectroscopy & Radiative Transfer*, 97(3), 317–331. <https://doi.org/10.1016/j.jqsrt.2005.04.015>
- Park, S., Western, L. M., Saito, T., Redington, A. L., Henne, S., Fang, X., et al. (2021). A decline in emissions of CFC-11 and related chemicals from eastern China. *Nature*, 590(7846), 433–437. <https://doi.org/10.1038/s41586-021-03277-w>
- Pincus, R., Buehler, S. A., Brath, M., Crevoisier, C., Jamil, O., Evans, K. F., et al. (2020). Benchmark calculations of radiative forcing by greenhouse gases. *Journal of Geophysical Research: Atmosphere*, 123(23), e2020JD033483. <https://doi.org/10.1029/2020JD033483>
- Pincus, R., Forster, P. M., & Stevens, B. (2016). The radiative forcing model intercomparison project (RFMIP): Experimental protocol for CMIP6. *Geoscientific Model Development*, 9(9), 3447–3460. <https://doi.org/10.5194/gmd-9-3447-2016>
- Pinnock, S., Hurley, M. D., Shine, K. P., Wallington, T. J., & Smyth, T. J. (1995). Radiative forcing of climate by hydrochlorofluorocarbons and hydrofluorocarbons. *Journal of Geophysical Research*, 100(D11), 23227–23238. <https://doi.org/10.1029/95JD02323>
- Rinsland, C. P., Goldman, A., Murcray, D. G., Murcray, F. J., Bonomo, F. S., Blatherwick, R. D., et al. (1985). Tentative identification of the $780\text{-cm}^{-1} \nu_4$ band q branch of chlorine nitrate in high-resolution solar absorption spectra of the stratosphere. *Journal of Geophysical Research*, 90(D5), 7931–7943. <https://doi.org/10.1029/jd090id05p07931>
- Sharpe, S. W., Johnson, T. J., Sams, R. L., Chu, P. M., Rhoderick, G. C., & Johnson, P. A. (2004). Gas-phase databases for quantitative infrared spectroscopy. *Applied Spectroscopy*, 58(12), 1452–1461. <https://doi.org/10.1366/0003702042641281>
- Shine, K., & Myhre, G. (2020). The spectral nature of stratospheric temperature adjustment and its application to halocarbon radiative forcing. *Journal of Advances in Modeling Earth Systems*, 12(3), e2019MS001951. <https://doi.org/10.1029/2019MS001951>
- Sihra, K., Hurley, M. D., Shine, K. P., & Wallington, T. J. (2001). Updated radiative forcing estimates of 65 halocarbons and nonmethane hydrocarbons. *Journal of Geophysical Research*, 106(D17), 20493–20505. <https://doi.org/10.1029/2000JD900716>
- Soden, B. J., & Held, I. M. (2006). An assessment of climate feedbacks in coupled ocean-atmosphere models. *Journal of Climate*, 19(14), 3354–3360. <https://doi.org/10.1175/JCLI3799.1>
- Wallington, T. J., Pivesso, B. P., Lira, A. M., Anderson, J. E., Nielsen, C. J., Andersen, N. H., & Hodnebrog, Ø. (2016). CH_3Cl , CH_2Cl_2 , CHCl_3 , and CCl_4 : Infrared spectra, radiative efficiencies, and global warming potentials. *Journal of Quantitative Spectroscopy and Radiative Transfer*, 174(Supplement C), 56–64. <https://doi.org/10.1016/j.jqsrt.2016.01.029>